Draft version December 6, 2019
Typeset using LaTeX **twocolumn** style in AASTeX63

RELICS: A Very Large ($\theta_E \sim 40''$) Cluster Lens – RXC J0032.1+1808

Ana Acebron,[1] Adi Zitrin,[1] Dan Coe,[2] Guillaume Mahler,[3] Keren Sharon,[3] Masamune Oguri,[4,5,6] Maruša Bradač,[7] Larry D. Bradley,[2] Brenda Frye,[8] Christine J. Forman,[9] Victoria Strait,[7] Yuanyuan Su,[10] Keiichi Umetsu,[11] Felipe Andrade-Santos,[9] Roberto J. Avila,[2] Daniela Carrasco,[12] Catherine Cerny,[13] Nicole G. Czakon,[11] William A. Dawson,[14] Carter Fox,[3] Austin T. Hoag,[7] Kuang-Han Huang,[7] Traci L. Johnson,[3] Shotaro Kikuchihara,[15,16] Daniel Lam,[17] Lorenzo Lovisari,[9] Ramesh Mainali,[8] Mario Nonino,[18] Pascal A. Oesch,[19] Sara Ogaz,[2] Masami Ouchi,[20,21] Matthew Past,[3] Rachel Paterno-Mahler,[3] Avery Peterson,[3] Russell E. Ryan,[2] Brett Salmon,[2] Daniel P. Stark,[8] Sune Toft,[22,23] Michele Trenti,[12,24] Benedetta Vulcani,[25] and Brian Welch[26]

[1] *Physics Department, Ben-Gurion University of the Negev, P.O. Box 653, Be'er-Sheva 8410501, Israel*
[2] *Space Telescope Science Institute, 3700 San Martin Drive, Baltimore, MD 21218, USA*
[3] *Department of Astronomy, University of Michigan, 1085 South University Ave, Ann Arbor, MI 48109, USA*
[4] *Research Center for the Early Universe, University of Tokyo, Tokyo 113-0033, Japan*
[5] *Department of Physics, University of Tokyo, Tokyo 113-0033, Japan*
[6] *Kavli Institute for the Physics and Mathematics of the Universe (Kavli IPMU, WPI), University of Tokyo, Chiba 277-8582, Japan*
[7] *Department of Physics, University of California, Davis, CA 95616, USA*
[8] *Department of Astronomy, Steward Observatory, University of Arizona, 933 North Cherry Avenue, Tucson, AZ, 85721, USA*
[9] *Harvard-Smithsonian Center for Astrophysics, 60 Garden Street, Cambridge, MA 02138, USA*
[10] *Department of Physics and Astronomy, University of Kentucky, 505 Rose Street, Lexington, KY, 40506, USA*
[11] *Academia Sinica Institute of Astronomy and Astrophysics (ASIAA), No. 1, Section 4, Roosevelt Road, Taipei 10617, Taiwan*
[12] *School of Physics, University of Melbourne, VIC 3010, Australia*
[13] *Astronomy Department and Institute for Astrophysical Research, Boston University, 725 Commonwealth Ave., Boston, MA 02215, USA*
[14] *Lawrence Livermore National Laboratory, P.O. Box 808 L-210, Livermore, CA, 94551, USA*
[15] *Institute for Cosmic Ray Research, The University of Tokyo, 5-1-5 Kashiwanoha, Kashiwa, Chiba 277-8582, Japan*
[16] *Department of Astronomy, Graduate School of Science, The University of Tokyo, 7-3-1 Hongo, Bunkyo, Tokyo, 113-0033, Japan*
[17] *Leiden Observatory, Leiden University, NL-2300 RA Leiden, The Netherlands*
[18] *INAF - Osservatorio Astronomico di Trieste, Via Tiepolo 11, I-34131 Trieste, Italy*
[19] *Department of Astronomy, University of Geneva, Chemin des Maillettes 51, 1290 Versoix, Switzerland*
[20] *26Institute for Cosmic Ray Research, The University of Tokyo, 5-1-5 Kashiwanoha, Kashiwa, Chiba 277-8582, Japan*
[21] *Kavli Institute for the Physics and Mathematics of the Universe (Kavli IPMU, WPI), University of Tokyo, Kashiwa, Chiba 277-8583, Japan*
[22] *Cosmic Dawn Center (DAWN)*
[23] *Niels Bohr Institute, University of Copenhagen, Lyngbyvej 2, DK-2100, Copenhagen, Denmark*
[24] *Australian Research Council, Centre of Excellence for All Sky Astrophysics in 3 Dimensions (ASTRO 3D), Melbourne VIC, Australia*
[25] *INAF-Osservatorio Astronomico di Padova, Vicolo Dellosservatorio 5, 35122 Padova Italy*
[26] *Department of Physics and Astronomy, The Johns Hopkins University, 3400 North Charles Street, Baltimore, MD 21218, USA*

(Received; Revised; Accepted)

Submitted to ApJ

ABSTRACT

Extensive surveys with the *Hubble Space Telescope* (HST) over the past decade, targeting some of most massive clusters in the sky, have uncovered dozens of galaxy-cluster strong lenses. The massive cluster strong-lens scale is typically $\theta_E \sim 10''$ to $\sim 30-35''$, with only a handful of clusters known with Einstein radii $\theta_E \sim 40''$ or above (for a source at $z_s \sim 2$, nominally). Here we report another very large cluster lens, RXC J0032.1+1808 (at $z = 0.3956$), the second richest cluster in the redMapper cluster catalog and the 85th most massive cluster in the Planck Sunyaev-Zel'dovich catalog. With both our

Corresponding author: Ana Acebron
anaacebronmunoz@gmail.com

Light-Traces-Mass and fully parametric (dPIEeNFW) approaches, we construct strong lensing models based on 18 multiple images of 5 background galaxies in the *HST* data from the *Reionization Lensing Cluster Survey* (RELICS; using also data also from a previous snapshot program), in addition to a previously found sextuply imaged system in this cluster. Furthermore, we compare these models to the Lenstool and GLAFIC models, which were produced independently as part of the RELICS program. All models reveal a large effective Einstein radius of $\theta_E \simeq 40''$ ($z_s = 2$). The central region of the cluster shows an obvious concentration of substructures, which together account for the large critical area. Although RXC J0032.1+1808 has a very large critical area and lensing strength, only three magnified high-redshift candidates are found within the field targeted by RELICS. Nevertheless, given its exceptional lensing strength, we expect many more high-redshift candidates will be seen in an additional coverage with *HST*, and in deeper, longer-wavelength observations with *JWST*.

Keywords: galaxies: clusters: general — galaxies: clusters: individual (RXC J0032.1+1808, MACS J0032.1+1808) — gravitational lensing: strong

1. INTRODUCTION

Over the past decade, extensive galaxy cluster lensing campaigns have been undertaken with the *Hubble Space Telescope* (HST; Postman et al. 2012; Schmidt et al. 2014; Treu et al. 2015; Lotz et al. 2017; Coe et al. 2019, Steinhardt et al. in preparation). *HST*'s unique combination of sensitivity and resolution allows for the identification of multiply imaged galaxies lensed by the targeted galaxy clusters (see for instance Franx et al. 1997; Frye & Broadhurst 1998; Broadhurst et al. 2005; Diego et al. 2018; Jauzac et al. 2019; Caminha et al. 2019; Lagattuta et al. 2019). These multiple images, in turn, allow us to construct mass models for the clusters, describing the underlying matter distribution. Most (albeit not all) of the clusters targeted with *HST*, which are typically estimated to be massive based on X-ray, the Sunyaev-Zeldovich effect (SZ, Sunyaev & Zeldovich 1970), or optical richness criteria (and lensing signatures such as giant arcs in ground based data), show multiply imaged background galaxies in numbers that generally increase with strong lens scale (or critical area, i.e. the area enclosed by the critical curves of infinite magnification; see for instance Vega-Ferrero et al. 2019).

Following the high projected mass densities in their centres, the strong-lens scale of galaxy cluster lenses typically reaches θ_E of the order of tens of arcseconds, with θ_E being the effective Einstein radius (i.e., the radius of the area enclosed by the critical curves, were it a circle). This indeed is the range of typical Einstein radii found in lensing analyses of well-known clusters (Richard et al. 2010b; Oguri et al. 2012; Zitrin et al. 2015). Since the Einstein radius size essentially depends on the mass enclosed in the core of the cluster, the distribution of Einstein radii can be used to probe cosmological models as well as structure formation and evolution in its framework (Turner et al. 1984; Narayan & White 1988; Oguri & Blandford 2009). Due to the shape of the cosmic mass function (Tinker et al. 2008), more massive clusters and thus, generally, larger Einstein radii become rarer (see for instance Oguri et al. 2012; Zitrin et al. 2012). Indeed, only a handful of clusters are known to have Einstein radii of $\theta_E \gtrsim 35''$, for a source at $z_s \sim 2$, nominally (see Table 1). The number of clusters with particularly large Einstein radii is therefore very important, because it can place useful constraints on structure formation and evolution models (e.g. Oguri & Blandford 2009).

The *Reionization Lensing Cluster Survey* (RELICS; PI: Coe; Coe et al. 2019) is a large *Hubble Space Telescope* program that has observed 41 galaxy clusters chosen largely based on SZ-mass estimates from the Planck PSZ2 all-sky catalog (Planck Collaboration et al. 2016). One of the chief goals of the RELICS survey is to identify bright high-redshift galaxies that could be followed up from the ground and with the upcoming *James Webb Space Telescope* (*JWST*). Lens models for the observed clusters are needed to study the dark matter distribution, as well as the the intrinsic properties of newly uncovered high-redshift galaxy candidates lensed by these clusters (Salmon et al. 2017, 2018).

In our systematic analysis of RELICS clusters (Cerny et al. 2018; Acebron et al. 2018, 2019; Cibirka et al. 2018; Paterno-Mahler et al. 2018; Mahler et al. 2019), we have analyzed RXC J0032.1+1808[1] (Böhringer et al. 2001; Ebeling et al. 2001), located at R.A. = 00h32m11.0s, Decl = +18d07m49.0s at a redshift of $z = 0.3956$. RXC J0032.1+1808 (RXC0032 hereafter) is the second richest galaxy cluster in the SDSS DR8 redMaPPer cluster catalog (only after RMJ224319.8-093530.9; see Rykoff et al. 2014), but only the 85th most massive cluster in the PSZ2 catalog (Planck Collaboration et al. 2016), with a mass of $M_{500} = 7.61^{+0.57}_{-0.63} \times 10^{14} M_\odot$, where M_{500} is de-

[1] Also known as PSZ1 G116.48-44.47, WHL J8.03426+18.10 and MACS J0032.1+1808.

Table 1. Known strong lensing clusters with Einstein radius above $\theta_E > 35$" ($z_s = 2$)†.

Galaxy cluster name	R.A. [J2000]	Decl [J2000]	z	θ_E[a]	Surveys[b]	References[c]
MACS J0717.5+3745	07:17:34	+37:44:49	0.5460	$\sim 55''$	HFF[d], CLASH[e], BUFFALO[f]	Zitrin et al. (2009)
Abell 1689	13:11:34	-01:21:56	0.1890	$\sim 45''$	-	Broadhurst et al. (2005)
PLCK G287.0+32.9	11:50:49	-28:05:07	0.3800	$\sim 42''$	RELICS[g]	Zitrin et al. (2017)
RXCJ2211.7-0349	22:11:43	-03:49:45	0.3970	$\sim 41''$	RELICS	Cerny et al. (2018)
Abell 370	02:39:53	-01:34:36	0.3750	$\sim 39''$	HFF, BUFFALO	Richard et al. (2010a)
RXC J0032.1+1808	00:32:11	+18:07:49	0.3956	$\sim 40''$	RELICS	This work
PLCK G171.9-40.7	03:12:57	+08:22:19	0.2700	$\sim 37''$	RELICS	Acebron et al. (2018)
RCS2 J232727.6-020437	23:27:08	-02:04:54	0.6986	$\sim 35''$	RELICS	Sharon et al. (2015)

[a] The Einstein radii are obtained from strong lensing analyses using different algorithms.

[b] Recent *HST* lensing surveys that included the cluster.

[c] First strong-lensing analysis to publish the size of the lens. More references are available in the literature for some of the clusters.

[d] *Hubble Frontier Fields* Survey; see Lotz et al. (2017)

[e] *Cluster Lensing And Supernova Survey with Hubble*; see Postman et al. (2012)

[f] *Beyond Ultra-deep Frontier Fields and Legacy Observations* Survey; see Steinhardt et al. (in prep)

[g] Coe et al. (2019)

† We note that there are other clusters that were claimed to have large Einstein radii, but were later downsized in updated analyses. For example, both MACS J2129.4-0741 and MACS J0257.1-2325 were reported by Zitrin et al. (2011) to have Einstein radii above $35''$, yet an updated analysis with additional broadband data (Zitrin et al. 2015, and *in preparation*, respectively) suggests these are smaller lenses. As another example, RX J1347-1145 was analyzed by Halkola et al. (2008) to have an Einstein radius above $35''$as well. An updated analysis using CLASH data by Zitrin et al. (2015), resulted in a somewhat smaller value of $\theta_E \sim 33''$ for a redshift $z_s = 2.0$.

fined as the cluster mass within the radius R_{500} inside which the mean mass-density is 500 times the critical density δ_c. Our strong lensing (SL) analysis of RXC0032 has revealed a very large critical area, similar to only a handful of other clusters known to date (see Table 1). In this work, we report this discovery and detail our SL modeling.

The outline of the paper is as follows: in Section 2 we briefly describe the data and observations used to identify multiple images for the SL analysis, which is presented in Section 3. The results are shown and discussed in Section 4. We compare our results with those obtained from the Lenstool and GLAFIC pipelines[2] in Section 5 before summarizing our work in Section 6. Throughout we assume a ΛCDM cosmology with $\Omega_{m0} = 0.3$, $\Omega_{\Lambda 0} = 0.7$, $H_0 = 70$ km s^{-1}Mpc^{-1} where $1'' = 5.337$ kpc at the redshift of RXC J0032.1+1808.

[2] The Lenstool and GLAFIC models are also publicly available through MAST[3].

2. DATA AND OBSERVATIONS

RXC0032 is part of the RELICS cluster sample (Coe et al. 2019). Each cluster field in the RELICS program was observed for 2 orbits with *Wide Field Camera 3* (WFC3/IR) in F105W, F125W, F140W, and F160W, and complemented archival observations with the *Advanced Camera for Surveys* (ACS) so that each field is observed for 3 orbits – one in each of the passbands F435W, F606W, and F814W. In addition, 30 hours per band in each of the *Spitzer*-IRAC channels (PI: M. Bradac, PI: Soifer) were observed. As one orbit of *HST* archival observations already existed for RXC0032 (program GO 12166, PI: Ebeling), RELICS observed this galaxy cluster for only 2 orbits with each of the ACS bands, in addition to the two WFC3 orbits (Coe et al. 2019).

Data reduction of the HST images is described in Coe et al. (2019). We used the photometric source catalogs generated with Source Extractor (Bertin & Arnouts 1996) in dual-image mode from the final drizzled 0.06"/pixel images. The photometric redshifts we

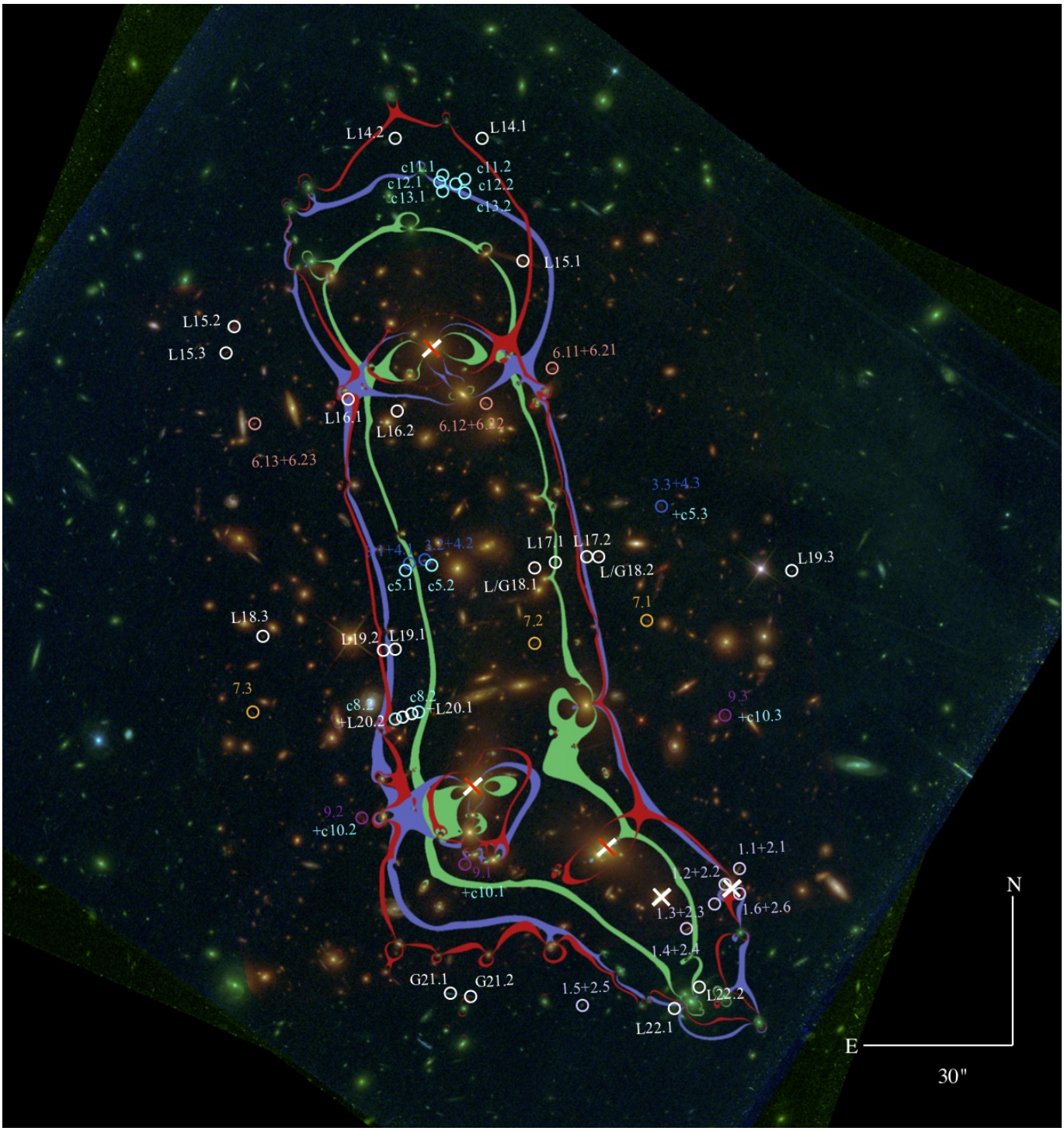

Figure 1. Color-composite RGB image of RXC0032. The image was constructed with the *HST/ACS* passbands F435W (blue), a combination of F606W+F814W (green), and a combination of the *HST/WFC3IR* passbands F105W+F125W+F140W+F160W (red). The resulting critical curves from our best-fit LTM model are displayed for a source at $z = 2.0$ (in green) and $z = 9.0$ (in violet). In addition, we add the critical lines at $z = 9.0$ from our fully parametric best-fit dPIEeNFW model (in red). Multiple images (color coded to ease their identification) are numbered according to Table A1. Cyan systems are reported as candidates and not used in the LTM/dPIEeNFW models. White systems are those reported by the Lenstool and/or GLAFIC modeling teams. White crosses indicate cluster members whose weight is freely optimized in the LTM model whereas the half-red crosses identify the location of the large-scale dark matter halos for the dPIEeNFW model.

use (hereafter z_{phot}), were derived using the *Bayesian Photometric Redshift* program (BPZ, Benítez 2000; Benítez et al. 2004; Coe et al. 2006) from seven *HST* band imaging-data (from the combined RELICS and the aforementioned archival *HST* data). The reduced imaging, catalogs, and data products are available for the community through the Mikulski Archive for Space Telescopes (MAST)[3].

3. STRONG LENSING FORMALISM

We construct lens models for RXC0032 using two methodologies. Primarily, we use the Light-Traces-mass (LTM) methodology, outlined in Zitrin et al. (2015) (and references therein); see also Broadhurst et al. (2005). With this methodology we uncover multiple image sets and publish the first estimate for the size of the lens. We also use for comparison a fully parametric formalism, dubbed hereafter dPIEeNFW. Both methodologies assume two main mass components for the mass distribution: one that accounts for the cluster galaxies, and a second which represents the dark matter distribution. While member galaxies and hence the member-galaxies component are also represented differently, the main difference between the two methodologies is that in the LTM methodology the dark matter distribution is assumed to follow the light distribution, whereas in the parametric model it is independent and follows a combination of symmetric analytic forms. Both methodologies are implemented on a grid where the resolution can be changed for computational time purposes. In the case of RXC0032's models, we have assumed a resolution 4 times larger along each axis than that of the RELICS *HST* observations of $0.06''$. Both methodologies are implemented in the same pipeline (Zitrin et al. 2015), and are briefly detailed below.

3.1. *LTM*

The LTM formalism is based on the assumption that the cluster member luminosity-weighted distribution is a reasonable tracer for the dark matter component in the cluster. The model is constructed from a component representing the cluster galaxies, in which each galaxy is assigned a power-law surface density mass distribution, scaled by its luminosity. The exponent is the same for all galaxies and the superposition of all galaxy contributions constitutes the member-galaxies component of the model. This map is then smoothed with a Gaussian kernel to represent the DM distribution component. The two components are then added with a relative weight

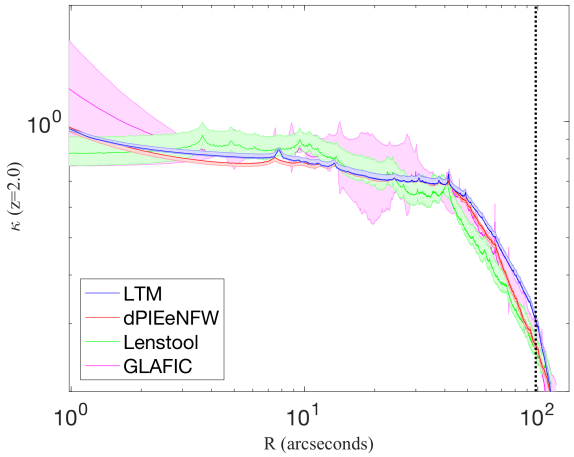

Figure 2. Convergence profiles from our best-fit LTM and dPIEeNFW models, scaled to a source redshift of $z = 2.0$. Also plotted for comparison are the Lenstool and GLAFIC models (see Section 5). All profiles are obtained by radially averaging the convergence map in radial annuli, centered on R.A=8.046202; Decl=18.132533. The vertical dashed line indicates the area in which multiple images have been identified.

and scaled to match a multiple image system (or redshift) of choice. This basic model includes only four free parameters: the power-law exponent for the mass distribution of the cluster galaxies, the smoothing Gaussian width, the galaxy to dark matter (DM) weight, and the overall normalization. In addition, we typically include a two-parameter external shear to add further flexibility (manifested mainly in the form of ellipticity of the critical curves), bringing the number of free parameters to six. It is also to leave some galaxy masses to be independently scaled - especially for brighter cluster galaxies, for which we typically find the mass to light (M/L) ratio to be a few times higher than that of other cluster members. These key galaxies can also be assigned an ellipticity, and a core. Finally, the redshifts of systems with no spectroscopic redshift can be optimized by the lens model.

3.2. *dPIEeNFW*

Our parametric formalism is based on analytic functions for both the member-galaxies and the DM components. Galaxy-scale halos are parametrized each as a double pseudo-isothermal elliptical (dPIE) mass distribution [4] (see for instance Elíasdóttir et al. 2007). Their

[3] https://archive.stsci.edu/prepds/relics/

[4] In previous analyses with this pipeline the naming used for the galaxy component was PIEMD, which stands for a *pseudo-isothermal elliptical mass distribution*; the dPIE is a combination of two PIEMDs – which is what we incorporate in practice.

velocity dispersion, core radius and cut-off radius are scaled based on their luminosity following scaling relations found to describe well early-type galaxies and scaled with respect to a reference luminosity value of the typical luminosity of a galaxy at the cluster's redshift (Jullo et al. 2007; Monna et al. 2015; Bergamini et al. 2019). All cluster galaxies, aside from the few brightest cluster galaxies in the cluster core, have no ellipticities assigned to them and their positional parameters are fixed to those derived from their light distribution. Each large-scale DM halo is represented by an elliptical Navarro Frenk and White mass distribution (eNFW, Navarro et al. 1996) where their concentration, mass, ellipticity, and position angle are free parameters of the model. The central positions of the NFW halos can also be freely optimized but here they are fixed to the light centroid of the brightest cluster galaxies.

3.3. *Minimization*

For both methodologies, the best-fitting model parameters are found by minimizing the distance in the image-plane between the observed and model-predicted positions of the multiple-image centres, via a χ^2 criterion (the equations for the χ^2 and RMS calculations are presented in Acebron et al. 2019). To do so, we use a Monte Carlo Markov Chain (MCMC) engine with a Metropolis-Hastings algorithm that typically includes several thousand steps after the burn-in phase, from which both the best-fit model and the uncertainties are derived. We consider for both models a positional uncertainty of $1.4''$. This value has been found to encompass both the underlying statistical uncertainties, the systematic uncertainties between our LTM and dPIEeNFW methods, as well as possible uncertainties arising from structure along the line of sight (Host 2012). For more details on the modeling scheme see Zitrin et al. (2015) and references therein.

3.4. *Strong lensing analysis of RXC J0032.1+1808*

The starting point of our modeling relies on the construction of a cluster member catalog based on the red-sequence method (Gladders & Yee 2000). We use the magnitudes measured from the F606W and F814W filters to draw a color-magnitude diagram. We only considered galaxies down to 24 AB within ± 0.3 mag of the sequence (De Lucia & Helmi 2008). To exclude stars from our selection we do not include objects whose magnitudes are brighter than 17 AB or have a *stellarity* index below < 0.95. In addition, we take advantage of the delivered photometric catalog by RELICS to check that all selected cluster members were within $z_{phot} \pm 0.1$ of the mean redshift of the cluster (as measured by the BPZ software). We finally perform a visual inspection of the selected cluster members. This allows us to discard further interloping galaxies (bright foreground galaxies for instance) or artifacts (such as faint and diffuse objects or double detections), or add missing galaxies that appear to be cluster members based on their colors (due to the strict magnitude cuts applied).

We identify several multiply imaged background galaxies used in the SL modeling as well as candidate identifications that we present hereafter. All systems are labeled according to Table A1 and Figure 1. The first multiply imaged system used to build a SL mass model was reported by Dessauges-Zavadsky et al. (2017) using the single orbit of *ACS* imaging obtained prior to RELICS together with data from *Herschel*, *Spire*, the Plateau de Bure Interferometer (PdBI) and the Jansky Very Large Array (JVLA). They measured the spectroscopic redshift of this system to be $z = 3.6314$. They identified six two-knot images belonging to the system (labeled as systems 1 and 2 in Table A1). Based on the full *HST ACS + WFC3/IR* dataset including RELICS imaging, we detected additional multiply imaged systems (without a spectroscopic confirmation yet), which we identify based on their morphology and color similarity and include as lensing constraints in our models. Systems 3, 4 and c5 straddle the critical curve each forming two bright knots stretching into an arc with their counter-images on the opposite side of the cluster. System 6 is lensed into three images appearing as two distinct pink and blue knots (systems 6.1 and 6.2 in our modelling) in the composite *HST ACS* and *WCF3/IR* images (Figure 1), making this identification reliable. System 7 is lensed into three images which are identified mainly thanks to their similar, red dropout colors as they do not present any peculiar morphology. This system is a relatively high-redshift dropout object ($z_{phot} \sim 4.41$ based on its first image for which the photometric redshift is the most reliable), hence its redshift is assumed correct and we fix it in our model. Finally, system 9 is lensed into three diffused red images (in the *ACS* and *WFC3* composite image). We also identify additional, potential systems that were however not included in our SL modeling as constraints. System c8 appears to be lensed into two images straddling the critical curve. We do not however identify a third counter-image on the other side of the critical curves so we report it as a candidate system. System c10 lies next to system 9 and is comprised of two faint emission knots. Our SL models predict additional counterimages near a group of cluster member galaxies located at R.A=8.0470889; Decl=18.117521. However due to the light contamination we cannot make a re-

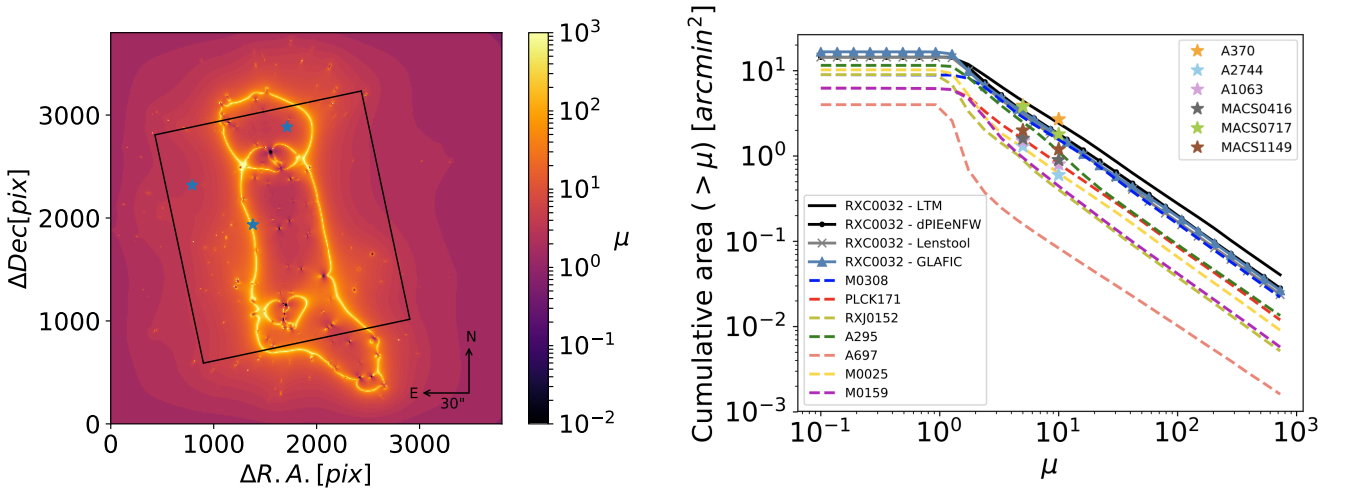

Figure 3. Left panel: Magnification map from our best-fit LTM model for a source at $z_s = 9$ in which the RELICS high-z candidates found by Salmon et al. (2017) are marked as blue stars. The black rectangle indicates the WFC3/IR FOV.
Right panel: Cumulative area having a magnification higher than a given value for a source at $z_s = 9.0$ in RXC0032's field from our LTM and dPIEeNFW, Lenstool and GLAFIC best fit models. For comparison, we also show the lensing strengths from other RELICS SL clusters modeled with the LTM pipeline, MACS J0308.9+2645, PLCK G171.9-40.7 and Abell S295, Abell 697, MACS J0025.4-1222, MACS J0159.8-0849 and RXJ0152.7-135. The cumulative areas ($\mu > 5$ and $\mu > 10$) for the *Hubble Frontier Fields* clusters are also indicated as colored stars, computed from the submitted ZITRIN-LTM-GAUSS models. The 1σ errors are typically of the size of the star symbol. We note that different clusters have been modeled with different fields-of-view.

liable identification. Systems c11, c12 and c13 consist of two arcs straddling the critical curve in the northern region of the cluster. Lacking a *WFC3/IR* coverage in that northern area of the cluster, and BPZ yielding significantly different photometric redshift estimates we decided to keep these systems as candidate systems. A spectroscopic confirmation of these system would help to more accurately constrain the mass distribution in the most northern region, where no other lensing constraints are seen.

- **LTM**:

  The LTM model is built by considering the weight of the 5 brightest cluster members (identified as white crosses in Figure 1) as free parameters, i.e. allowing their mass-to-light (M/L) ratio to vary. We also consider the ellipticity (varying within a flat, small prior of ± 0.05) and position angle (varying within $\pm 5°$) of the bright galaxies located at R.A=8.04691; Decl=18.118922, and R.A=8.039185; Decl=18.115616, as free parameters.
  We scale our model to the spectroscopic redshift of systems 1 and 2 (see Table A1). The redshift of the remaining systems, except dropout system 7, are left as free parameters to be optimized in the minimization procedure (allowing the relative D_{LS}/D_S ratio for each system, corresponding to its best-fit z_{phot} value, to vary by up to ± 0.05).
  Taking into account the additional freely optimized cluster members and source redshifts, our final model includes a total of 20 free parameters. The resulting critical curves (for a source at $z_s = 2$ and $z_s = 9$) for our final best-fit model which has an image reproduction $RMS = 1.60''$, are shown in Figure 1.

- **dPIEeNFW**: In merging clusters such as the one analyzed here, multiple DM halos are usually incorporated in the modeling in order to better explain the mass distribution. Our best-fit model comprises three large-scale DM halos whose centres are indicated in Figure 1 as half red crosses. The large-scale DM halos are parametrized with elliptical NFWs, where their ellipticity parameters, concentration and mass are optimized. Cluster members are modelled with a dPIE profile with a fixed core radius of 0.2 kpc, a velocity dispersion that is allowed to vary between 80 and 120 km/s, a cut radius varying from 45 kpc to 65 kpc. They are modeled as spherical with a mag0 = -21.56 (a reference magnitude for the scaling relations; Faber & Jackson 1976). Similarly as in the LTM model, we leave the ellipticities and position angles of the two bright galaxies presented above to be optimized.
  We adopt the same multiple images and cluster

member catalogs as for the LTM model, leaving as free parameters the redshifts of background sources that have not been spectroscopically confirmed (except for system 7). Our final model includes a total of 24 free parameters. Our best-fit model has an image reproduction of $RMS = 1.65''$ and for comparison, we also show in Figure 1 the resulting critical curves for a source at $z_s = 9$.

4. RESULTS AND DISCUSSION

Figure 1 shows the critical curves from our lens models. Both the LTM and dPIEeNFW models, despite having a very different representation for the different mass components, yield overall similar critical curves. This is perhaps somewhat expected, given that similar sets of multiple images were used as constraints, although notable differences exist as well - especially in regions of high magnification or regions with less constraints.

Figure 2 shows the convergence profile for RXC0032. The SL region is dominated by a large number of substructures (accounting for the shallow inner profile). We also note that the resulting mass distribution has a high overall elongation, or ellipticity, computed as $e = (a^2 - b^2)/(a^2 + b^2)$, of $e \sim 0.74(0.81) \pm 0.03$ from the LTM(dPIEeNFW) models.

We compute the value of the effective Einstein radius as $\theta_E = \sqrt{A/\pi}$, with A defined as the area enclosed within the critical curves. Our strong lensing analysis reveals a particularly prominent lens with a resulting Einstein radii of $\theta_E(z_s = 2) \sim 38.00''(40.2'') \pm 0.20''$ and $\theta_E(z_s = 9) \sim 47.3''(48.1'') \pm 0.25''$ from our LTM(dPIEeNFW) best-fit models, corresponding to an enclosed mass of $M(< \theta_E) = 2.10(2.73) \pm 0.2 \times 10^{14} M_\odot$ within the $z_s = 2$ critical curves. The high-degree of substructures aggregated in the center yields a very large Einstein radius, similar to only a few other clusters. While SZ signals, and gas probes in general, lead to the discovery of clusters with a high virial mass (Williamson et al. 2011; Planck Collaboration et al. 2016), a high total mass does not guarantee a large strong lensing region. RXC0032 portrays the loose relation – or at least the large scatter in the relation – between gas probes (and the SZ effect in particular) and the central strong lensing area, which depends more closely on various other factors (Giocoli et al. 2016) and especially the amount of matter concentrated or projected in the very center. In the case of RXC0032, it seems that the high cluster richness, for example, better traces the large Einstein radius.

We show in Figure 3 the $z_s = 9$ magnification map from our LTM best-fit model as well as the location of the detected high-redshift galaxy candidates within RXC0032's field-of-view covered by both ACS and WFC3 (Salmon et al. 2017). We compare in Table 2 the magnification estimates from both methods and provide the intrinsic M_{uv} at $\lambda = 1500\mathring{A}$ for the high-redshift candidates.

The derived lensing strength (in the right panel of Figure 3) shows that RXC0032 is a very prominent lens, with a large area of high magnification of about $\sim 4.4(3.4)$ arcmin^2 with $\mu > 5$ to $\sim 2.4(1.8)$ arcmin^2 with $\mu > 10$ from our LTM(dPIEeNFW) best-fit models. RXC0032's lensing strength is significantly larger than that of other RELICS clusters modeled with the LTM pipeline (Acebron et al. 2018, 2019; Cibirka et al. 2018) and similar or higher than those provided by most *Hubble Frontier Fields* (HFF) cluster lenses.

However, the field of RXC0032 seems to be a unique sightline, compared to similarly-strong cluster lenses. Despite its lensing strength and large critical area, RXC0032 reveals only three $z \sim 6$ high-redshift galaxy candidates detected in the field (Salmon et al. 2017); these are characterized in Table 2. RXJ0152.7-135 (RXJ0152 hereafter; Acebron et al. 2019) constitutes an interesting counter example. The strong lens modeling of both clusters, following the distribution of their member-galaxies, reveals two clusters with similar morphologies, i.e., very elongated and showing a high degree of substructure. These effects have been shown to significantly boost the cluster total cross-section (Meneghetti et al. 2007). This is clearly evident in the case of RXJ0152, which, despite being a much smaller lens ($\theta_E(z_s = 2) \sim 9''$; equivalent to a critical area of 0.06 arcmin^2), lenses 24 high-redshift galaxy candidates.

The field of RXC0032 provides the lowest yield of high-redshift candidates in comparison to those listed in the right panel of Figure 3. While such a small high-redshift candidate sample can be attributed to cosmic variance (Somerville et al. 2004; Trenti & Stiavelli 2008) especially as RELICS targets the brightest distant objects, the low number of high-redshift candidates could also be explained in part by the fact that the *HST/WFC3IR*'s field-of-view ($136'' \times 123''$) is fairly small compared to the size of the lens. In Figure 3 (left panel) we show that a significant proportion of high-magnification regions fall outside of the instrument's field-of-view.

The most interesting high-z candidate in this field is RXC0032+18-0571 (see Table 2), which lies in a very high-magnification area. In the composite (*ACS+WFC3*) image, this object appears as two distinct light emitting knots, one of which appears to be stretched into an $\sim 1.5''$ arc. This is in agreement with our lens model, which predicts a similar stretching for the arc, further supporting the high-z nature of this ob-

Table 2. High-z ($z \sim 6$) lensed candidates

Galaxy ID[a]	R.A. [deg]	Decl [deg]	J_{125} [b]	z_{phot}^{BPZ} [c]	z_{phot}^{EZ} [c]	μ^{LTM} [d]	$\mu^{dPIEeNFW}$ [d]	$\mu^{Lenstool}$ [d]	μ^{GLAFIC} [d]	$M_{uv,1500}$ [e]
RXC0032+18-0571	8.052543	18.131884	26.42 ± 0.25	$6.4^{+0.7}_{-0.8}$	$6.7^{+0.7}_{-1.5}$	$144.96^{+0.74}_{-1.00}$	$13.98^{+0.61}_{-0.62}$	$5.66^{+0.44}_{-0.39}$	$53.20^{+12.49}_{-61.73}$	$-14.97^{+0.32}_{-0.33}$
RXC0032+18-0052	8.046714	18.147703	26.07 ± 0.26	$5.5^{+0.2}_{-0.7}$	$5.8^{+0.2}_{-0.8}$	$5.88^{+0.06}_{-0.09}$	$3.64^{+0.06}_{-0.05}$	$0.78^{+0.12}_{-0.09}$	$2.74^{+0.38}_{-0.37}$	$-18.56^{+0.30}_{-0.32}$
RXC0032+18-0355	8.062891	18.138279	26.64 ± 0.28	$5.8^{+0.3}_{-5.1}$	$6.1^{+0.3}_{-5.3}$	$3.39^{+0.18}_{-0.22}$	$2.53^{+0.23}_{-0.20}$	$1.95^{+0.03}_{-0.04}$	$2.30^{+0.25}_{-0.22}$	$-18.67^{+0.31}_{-0.87}$

[a] Galaxy ID, following Salmon et al. (2017) notations.

[b] Apparent magnitude in the F125W band.

[c] Redshift estimation based on the BPZ and EAZY pipelines along with their 1σ uncertainties.

[d] Best-fit magnification estimates (at the respective source redshift) from the LTM, dPIEeNFW, Lenstool and GLAFIC models. The statistical uncertainty is computed as the standard deviation from 100 MCMC models. The LTM best-fit value is the one used for all relevant computations.

[e] Absolute magnitude, M_{uv}, at $\lambda = 1500$ Å for which the errors have been propagated from the photometric and magnification uncertainties based on our best-fit LTM model. The resulting rest-frame UV luminosities (corrected for lensing magnifications) have a mean of Muv $\sim$ -17.40 with a standard deviation of 2.10.

Table 3. Effective Einstein radius for RXC J0032.1+1808

Pipeline	$\theta_E(z_s = 2.0)$ [a] [']	$\theta_E(z_s = 9.0)$ [a] [']
LTM	38.00 ± 0.24	47.30 ± 0.25
dPIEeNFW	40.20 ± 0.20	48.10 ± 0.22
Lenstool	37.90 ± 0.18	46.00 ± 0.22
GLAFIC	42.20 ± 0.70	50.00 ± 0.80

[a] We note that the errors only represent the statistical uncertainty (computed from 100 random models). However, the systematic uncertainty is typically found to be $\sim 10\%$ which is represented by the scatter found between algorithms.

ject. Our SL models also predict a counter-image on the other side of the cluster. However, based on the RELICS high-z photometric study (Salmon et al. 2017), all apparent counter-image candidates have a lower photometric redshift estimate.

5. COMPARISON

As part of the RELICS survey, RXCJ0032 has also been modeled with the Lenstool (Jullo et al. 2007) and GLAFIC (Oguri 2010; Kawamata et al. 2016) pipelines whose high-end products are publicly available through the MAST archive[3]. In this Section we compare these two models to our modeling results. We give here a short summary of these two models and refer the reader to the references mentioned above for further details.

It should be noted that often in comparison studies, the same constraints are used throughout with the goal of comparing the different methodologies explicitly (e.g., Zitrin et al. 2015; Meneghetti et al. 2017). In contrast, here our goal is mainly to probe the credibility of our results and especially, the large Einstein radius estimation. We therefore incorporate the Lenstool and GLAFIC models as well, since these were constructed completely independently by other groups within the RELICS collaboration, including independently identified multiple image sets (presented in Table A1). The differences between the results of these different methods also provide the reader with a more quantitative assessment of the magnitude of underlying systematic uncertainties in the presented analysis. However, we note that while the image recovery RMS is often used in assessing the reliability of strong lens models, a comparison of the RMS values of models that use different constraints is of little use (e.g., Johnson & Sharon 2016).

- **Lenstool**: This model is built with 4 large-scale halos parametrised with a dPIE density profile. Their central coordinates, as well as their ellipticity, position angle, core radius and velocity dispersion, are left to be freely optimized. The small scale haloes associated to galaxy members, identified via the red-sequence method, are modelled with a dPIE profile with a fixed core radius of 0.15 kpc, while both the velocity dispersion and the cut radius are freely optimised and following the scaling relations (Faber & Jackson 1976; Jullo et al. 2007). The redshifts of all multiple images used in the modeling, but systems 1 and 2 with a spectroscopic redshift measurement, are freely op-

timized. All multiple images are included in the models with a positional uncertainty of $0.3''$ and the optimization is performed in the source plane. The best-fit model results in an image reproduction of $RMS = 1.34''$.

- **GLAFIC**: This model includes 4 elliptical NFW large-scale halos which have been fixed to the following coordinates: R.A, Decl= (8.049478, 18.143654); (8.047251, 18.116557); (8.039177, 18.115615); (8.040402, 18.123657) while the mass, ellipticity, position angle, and concentration parameters are left as free parameters. The SL model also includes cluster members identified with the red-sequence method that are modeled as pseudo-Jaffe ellipsoids (Keeton 2001) and following the scaling relations. The redshifts of all multiple images used in the GLAFIC SL model, but systems 1 and 2, are optimized assuming a Gaussian prior (with $\delta_z = 0.5$) around their photo-z estimates. A positional uncertainty of $0.6''$ is assumed for all multiple images. The GLAFIC best-fit model has an image reproduction of $RMS = 0.49''$.

We compare here the main outputs of our SL models, i.e., the convergence profile, magnification estimates, the resulting critical curves and Einstein radius.

We show in Figure 2 a comparison of all the convergence profiles. All convergence profiles are in good agreement within the 1σ error bars. However, the innermost region of the cluster is less well constrained, possibly due to uncertainties related to the chosen modeling techniques. Another notable issue is that the statistical uncertainties in the LTM and dPIEeNFW models are smaller than those in the Lenstool and GLAFIC models. We are in the process of examining the origin for this discrepancy, which might be, for instance, related to the finite and lower resolution of the LTM and dPIEeNFW models (which also tends to boost the official χ^2 quoted for them).

The resulting critical curves are found to be in good agreement between all models as shown in Figure 4. More significant differences are found in regions with no SL constraints such as the most northern or south-eastern regions of the cluster. We find that all modeling tools consistently reveal a large Einstein radius (see Table 3), with a mean and standard deviation estimates of $\theta_E(z_s = 2.0) = 39.60 \pm 2.05$ and $\theta_E(z_s = 9.0) = 47.90 \pm 1.70$.

All models do also estimate RXC0032 to have a prominent lensing strength and are in very good agreement regarding the total area with high magnification (see Figure 3 - right panel). However, as expected, large discrepancies between reconstructions appear around the lens critical lines, or the highest magnification regions (Meneghetti et al. 2017), as shown for the magnification estimates of the high-z candidates in Table 2. These values should thus be used with caution.

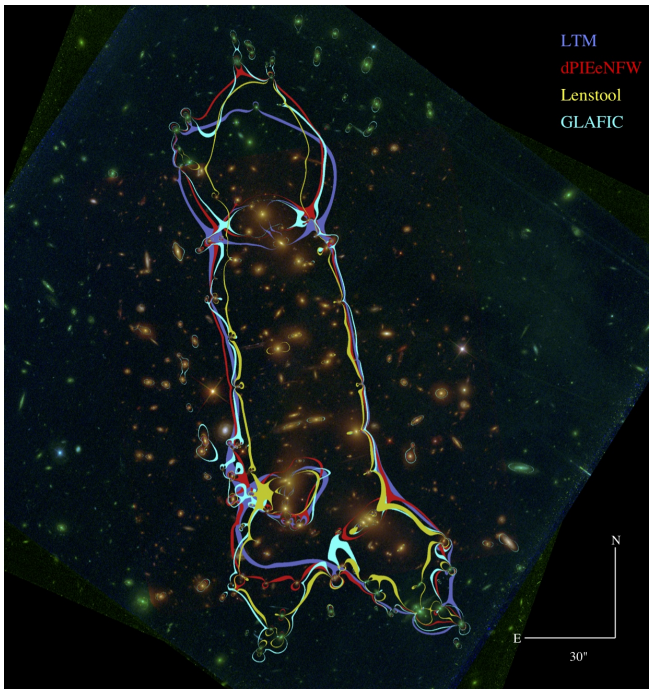

Figure 4. Comparison of the resulting critical curves from the best-fit LTM, dPIEeNFW, Lenstool and GLAFIC models for a source at $z = 9.0$ on a color-composite image of RXC0032.

Finally we note that all the SL models presented in this work have been built with only 2 multiply-imaged systems having a spectroscopic redshift confirmation. It will be interesting to revise the differences between the models when more secure redshifts are measured.

6. SUMMARY

The RELICS survey was designed to efficiently discover and characterize bright high-redshift galaxies magnified by massive cluster lenses, as well as to identify which galaxy clusters are the most efficient lenses for future follow-up campaigns (Coe et al. 2019). Based on RELICS observations, we present here a full SL analysis of the merging galaxy cluster RXC J0032.1+1808. More recently, efforts have focused on SL systematic uncertainties arising from different modeling techniques (Johnson & Sharon 2016; Meneghetti et al. 2017; Remolina González et al. 2018). In this work, we have adopted two different methodologies, the LTM technique and a fully parametric model, dPIEeNFW. We have also compared our results with the models obtained with the Lenstool and GLAFIC pipelines, that were

independently constructed, so that the results can be made more robust. As we show throughout, the results seem to agree fairly well between the different models. In that sense, differences between the LTM, dPIEeNFW, Lenstool and GLAFIC resulting models are then more representative of the true underlying uncertainties, than the magnitude of the statistical uncertainties from the respective minimization procedures.

The derived mass distribution and Einstein radius of RXC0032 reveals a very prominent lens, with a large effective Einstein radius of $\theta_E \sim 40''$ at $z_s = 2.0$, as supported by all models probed here. Since mergers enhance the lensing cross section, merging clusters such as RXC0032 are of particular interest for the statistical study of the strongest gravitational lenses and are particularly useful when comparing Einstein radius distributions from observations to those from theoretical expectations (Redlich et al. 2012, 2014). While RELICS has only uncovered three high-redshift galaxy candidates in this field (Salmon et al. 2017), we find that RXC0032 is a promising lens to carry out wider and deeper infrared imaging follow-up in order to expand the present coverage to all high-magnification regions.

All the lens models presented in this work and their corresponding deflection fields, magnification maps for different redshifts as well as a hundred MC random models to calculate errors, are made publicly available through the MAST archive[3].

This work is based on observations taken by the RELICS Treasury Program (GO-14096) with the NASA/ESA *HST*. Program GO-14096 is supported by NASA through a grant from the Space Telescope Science Institute, which is operated by the Association of Universities for Research in Astronomy, Inc., under NASA contract NAS5-26555. This work was performed in part under the auspices of the U.S. Department of Energy by Lawrence Livermore National Laboratory under Contract DE-AC52-07NA27344. This work was supported in part by World Premier International Research Center Initiative (WPI Initiative), MEXT, Japan, and JSPS KAKENHI Grant Number JP15H05892 and JP18K03693. K.U. acknowledges support from the Ministry of Science and Technology of Taiwan under the grant MOST 106-2628-M-001-003-MY3. This work is partially supported by the Australian Research Council Centre of Excellence for All-Sky Astrophysics in 3 Dimensions (ASTRO-3D). S.T. acknowledges support from the ERC Consolidator Grant funding scheme (project ConTExt, grant No. 648179). The Cosmic Dawn Center is funded by the Danish National Research Foundation.

Facilities: HST, Spitzer, MAST

REFERENCES

Acebron, A., Cibirka, N., Zitrin, A., et al. 2018, ApJ, 858, 42

Acebron, A., Alon, M., Zitrin, A., et al. 2019, ApJ, 874, 132

Benítez, N. 2000, ApJ, 536, 571

Benítez, N., Ford, H., Bouwens, R., et al. 2004, ApJS, 150, 1

Bergamini, P., Rosati, P., Mercurio, A., et al. 2019, A&A, 631, A130

Bertin, E., & Arnouts, S. 1996, A&AS, 117, 393

Böhringer, H., Schuecker, P., Guzzo, L., et al. 2001, A&A, 369, 826

Broadhurst, T., Takada, M., Umetsu, K., et al. 2005, ApJL, 619, L143

Caminha, G. B., Rosati, P., Grillo, C., et al. 2019, A&A, 632, A36

Cerny, C., Sharon, K., Andrade-Santos, F., et al. 2018, ApJ, 859, 159

Cibirka, N., Acebron, A., Zitrin, A., et al. 2018, ApJ, 863, 145

Coe, D., Benítez, N., Sánchez, S. F., et al. 2006, AJ, 132, 926

Coe, D., Salmon, B., Bradač, M., et al. 2019, ApJ, 884, 85

De Lucia, G., & Helmi, A. 2008, MNRAS, 391, 14

Dessauges-Zavadsky, M., Zamojski, M., Rujopakarn, W., et al. 2017, A&A, 605, A81

Diego, J. M., Schmidt, K. B., Broadhurst, T., et al. 2018, MNRAS, 473, 4279

Ebeling, H., Edge, A. C., & Henry, J. P. 2001, ApJ, 553, 668

Elíasdóttir, Á., Limousin, M., Richard, J., et al. 2007, arXiv e-prints, arXiv:0710.5636

Faber, S. M., & Jackson, R. E. 1976, ApJ, 204, 668

Franx, M., Illingworth, G. D., Kelson, D. D., van Dokkum, P. G., & Tran, K.-V. 1997, ApJL, 486, L75

Frye, B., & Broadhurst, T. 1998, ApJL, 499, L115

Giocoli, C., Bonamigo, M., Limousin, M., et al. 2016, MNRAS, 462, 167

Gladders, M. D., & Yee, H. K. C. 2000, AJ, 120, 2148

Halkola, A., Hildebrandt, H., Schrabback, T., et al. 2008, A&A, 481, 65

Host, O. 2012, MNRAS, 420, L18

Jauzac, M., Mahler, G., Edge, A. C., et al. 2019, MNRAS, 483, 3082

Johnson, T. L., & Sharon, K. 2016, ApJ, 832, 82
Jullo, E., Kneib, J.-P., Limousin, M., et al. 2007, New Journal of Physics, 9, 447
Kawamata, R., Oguri, M., Ishigaki, M., Shimasaku, K., & Ouchi, M. 2016, ApJ, 819, 114
Keeton, C. R. 2001, arXiv e-prints, astro
Lagattuta, D. J., Richard, J., Bauer, F. E., et al. 2019, MNRAS, 485, 3738
Lotz, J. M., Koekemoer, A., Coe, D., et al. 2017, ApJ, 837, 97
Mahler, G., Sharon, K., Fox, C., et al. 2019, ApJ, 873, 96
Meneghetti, M., Bartelmann, M., Jenkins, A., & Frenk, C. 2007, MNRAS, 381, 171
Meneghetti, M., Natarajan, P., Coe, D., et al. 2017, MNRAS, 472, 3177
Monna, A., Seitz, S., Zitrin, A., et al. 2015, MNRAS, 447, 1224
Narayan, R., & White, S. D. M. 1988, MNRAS, 231, 97p
Navarro, J. F., Frenk, C. S., & White, S. D. M. 1996, ApJ, 462, 563
Oguri, M. 2010, PASJ, 62, 1017
Oguri, M., Bayliss, M. B., Dahle, H., et al. 2012, MNRAS, 420, 3213
Oguri, M., & Blandford, R. D. 2009, MNRAS, 392, 930
Paterno-Mahler, R., Sharon, K., Coe, D., et al. 2018, ApJ, 863, 154
Planck Collaboration, Aghanim, N., Arnaud, M., et al. 2016, A&A, 594, A22
Postman, M., Coe, D., Benítez, N., et al. 2012, ApJS, 199, 25
Redlich, M., Bartelmann, M., Waizmann, J. C., & Fedeli, C. 2012, A&A, 547, A66
Redlich, M., Waizmann, J. C., & Bartelmann, M. 2014, A&A, 569, A34
Remolina González, J. D., Sharon, K., & Mahler, G. 2018, ApJ, 863, 60
Richard, J., Kneib, J. P., Limousin, M., Edge, A., & Jullo, E. 2010a, MNRAS, 402, L44
Richard, J., Smith, G. P., Kneib, J.-P., et al. 2010b, MNRAS, 404, 325
Rykoff, E. S., Rozo, E., Busha, M. T., et al. 2014, ApJ, 785, 104
Salmon, B., Coe, D., Bradley, L., et al. 2017, arXiv e-prints, arXiv:1710.08930
—. 2018, ApJL, 864, L22
Schmidt, K. B., Treu, T., Brammer, G. B., et al. 2014, ApJL, 782, L36
Sharon, K., Gladders, M. D., Marrone, D. P., et al. 2015, ApJ, 814, 21
Somerville, R. S., Lee, K., Ferguson, H. C., et al. 2004, ApJL, 600, L171
Sunyaev, R. A., & Zeldovich, Y. B. 1970, Ap&SS, 7, 3
Tinker, J., Kravtsov, A. V., Klypin, A., et al. 2008, ApJ, 688, 709
Trenti, M., & Stiavelli, M. 2008, ApJ, 676, 767
Treu, T., Schmidt, K. B., Brammer, G. B., et al. 2015, ApJ, 812, 114
Turner, E. L., Ostriker, J. P., & Gott, J. R., I. 1984, ApJ, 284, 1
Vega-Ferrero, J., Diego, J. M., & Bernstein, G. M. 2019, MNRAS, 486, 5414
Williamson, R., Benson, B. A., High, F. W., et al. 2011, ApJ, 738, 139
Zitrin, A., Broadhurst, T., Barkana, R., Rephaeli, Y., & Benítez, N. 2011, MNRAS, 410, 1939
Zitrin, A., Broadhurst, T., Bartelmann, M., et al. 2012, MNRAS, 423, 2308
Zitrin, A., Broadhurst, T., Rephaeli, Y., & Sadeh, S. 2009, ApJL, 707, L102
Zitrin, A., Fabris, A., Merten, J., et al. 2015, ApJ, 801, 44
Zitrin, A., Seitz, S., Monna, A., et al. 2017, ApJL, 839, L11

APPENDIX

A. LIST OF MULTIPLE IMAGES AND CANDIDATE IDENTIFICATIONS FOR RXC J0032.1+1808

Table A1. Multiple images and candidate identifications for RXC J0032.1+1808.

Arc ID[a]	R.A. [deg]	Decl [deg]	z_{phot} [z_{min}-z_{max}][b]	z_{spec}	z^{LTM}_{model}[68% C.I.][c]	$z^{dPIEeNFW}_{model}$[68% C.I.][c]	LTM/ dPIEeNFW[d]	Lenstool[d]	GLAFIC[d]	RMS[e] [']
1.1	8.031533	18.114345	0.24 [0.17-0.64]	3.6314[f]	-	-	✓	✓	✓	0.70
1.2	8.032142	18.113763	0.37 [0.27-0.43]	”	-	-	✓	✓	✓	0.70
1.3	8.032671	18.112831	0.31 [0.23-0.47]	”	-	-	✓	✓	✓	2.78
1.4	8.034162	18.111284	3.99 [0.25-4.36]	”	-	-	✓	✓	✓	0.77
1.5	8.040679	18.106825	0.44 [0.24-0.69]	”	-	-	✓	✓	✓	2.36
1.6	8.031840	18.113526	-	”	-	-	✓		✓	0.78
2.1	8.031454	18.114526	3.54 [3.42-3.65]	3.6314[g]	-	-				1.30
2.2	8.032260	18.113637	4.01 [3.90- 4.11]	”	-	-	✓	✓	✓	0.81
2.3	8.032492	18.113161	3.61 [3.55-3.74]	”	-	-	✓	✓	✓	1.96
2.4	8.034382	18.111196	3.61 [3.51-3.77]	”	-	-	✓	✓	✓	0.85
2.5	8.040661	18.106926	0.30 [0.11-3.61]	”	-	-	✓	✓	✓	2.29
2.6	8.031893	18.113509	-	”	-	-	✓		✓	0.57
3.1	8.050767	18.131576	1.05 [1.01-1.06]	-	2.48 [2.24-2.51]	2.22 [2.17-2.24]	✓	✓	✓	2.44
3.2	8.049925	18.131756	1.05 [1.01-1.76]	-			✓	✓	✓	0.56
3.3	8.035982	18.134820	1.63 [1.00-1.79]	-			✓		✓	0.99
4.1	8.051190	18.131482	-	-	2.32 [2.26-2.48]	2.06 [2.07-2.24]	✓		✓	0.64
4.2	8.049535	18.131823	-	-			✓		✓	3.35
4.3	8.036149	18.134948	0.97 [0.70-1.96]	-			✓		✓	0.35
c5.1	8.051015	18.131285	1.70 [1.58-1.78]	-	~ 2.3	~ 2.0			✓	-
c5.2	8.049483	18.131599	1.41 [1.39-1.81]	-					✓	-
c5.3	8.035952	18.134634	1.59 [1.13-1.92]	-					✓	-
6.11	8.042302	18.142446	1.71 [1.71-1.78]	-	1.50 [1.48-1.53]	1.81 [1.64-1.95]	✓	✓	✓	1.00
6.12	8.046450	18.140492	1.10 [1.02-1.14]	-			✓	✓	✓	0.73
6.13	8.059917	18.139378	1.11 [1.02-1.71]	-			✓	✓	✓	1.91
6.21	8.042491	18.142400	1.03 [0.93-1.09]	-	1.80 [1.77-1.93]	1.56 [1.53-1.57]	✓	✓	✓	0.34
6.22	8.046380	18.140578	-	-			✓	✓	✓	0.67
6.23	8.060023	18.139325	-	-			✓	✓	✓	1.33
7.1	8.036775	18.128377	4.41 [0.42-4.66]	-	4.4[f]	4.4[f]	✓	✓	✓	1.38

Table A1 *continued*

Table A1 *(continued)*

Arc ID[a]	R.A. [deg]	Decl [deg]	z_{phot} [z_{min}-z_{max}][b]	z_{spec}	z^{LTM}_{model}[68% C.I.][c]	$z^{dPIEeNFW}_{model}$[68% C.I.][c]	LTM/ dPIEeNFW[d]	Lenstool[d]	GLAFIC[d]	RMS[e] [']
7.2	8.043467	18.126995	0.30 [0.16-3.96]	-			✓	✓	✓	0.87
7.3	8.060019	18.123190		-			✓	✓	✓	2.64
c8.1	8.051712	18.122845	2.82 [2.74-3.11]	-	~ 2.7	~ 2.7		✓	✓	-
c8.2	8.049750	18.123512	0.05 [0.02-3.07]	-				✓	✓	-
9.1	8.047754	18.114628	3.25 [3.00-3.53]	-	3.28 [3.18-3.40]	2.05 [2.03-2.22]	✓	✓	✓	2.45
9.2	8.053467	18.117267	-	-			✓	✓	✓	2.16
9.3	8.032281	18.122876	2.14 [1.85-2.28]	-			✓	✓	✓	1.88
c10.1	8.053825	18.117562	2.32 [2.17-2.53]	-	~ 2.7	~ 2.2				-
c10.2	8.047263	18.114624	-	-						-
c10.3	8.032309	18.123215	-	-						-
c11.1	8.049167	18.153004	2.76 [0.07-3.08]	-	~ 3	~ 3		✓	✓	-
c11.2	8.047482	18.152860	2.71 [0.36-3.10]	-				✓	✓	-
c12.1	8.049383	18.152779	-	-	~ 3	~ 3				-
c12.2	8.048008	18.152721	1.36 [0.59-2.66]	-						-
c13.1	8.048654	18.152527	-	-	~ 3	~ 3				-
c13.2	8.047547	18.152442	1.54 [0.16-2.98]	-						-
L14.1	8.046523	18.155275	0.55 [0.46-4.54]	-	-	-		✓		-
L14.2	8.051645	18.155275	0.92 [0.75-1.42]	-	-	-		✓		-
L15.1	8.043844	18.148375	3.11 [0.26-3.32]	-	-	-		✓		-
L15.2	8.061134	18.144614	3.19[1.87-3.27]	-	-	-		✓		-
L15.3	8.061551	18.143318	2.40 [2.14-2.57]	-	-	-		✓		-
L16.1	8.054572	18.140649	-	-	-	-		✓		-
L16.2	8.051372	18.140131	-	-	-	-		✓		-
L17.1	8.040382	18.131975	4.23 [0.34-4.49]	-	-	-		✓		-
L17.2	8.042291	18.131664	0.77 [0.19-0.90]	-	-	-		✓		-
L/G18.1	8.039637	18.131971	2.64 [2.35-2.92]	-	-	-		✓	✓	-
L/G18.2	8.043413	18.131387	2.27 [2.22-2.55]	-	-	-		✓	✓	-
L18.3	8.059395	18.127467	2.31 [2.04-2.61]	-	-	-		✓		-
L19.1	8.051801	18.126669	3.94 [3.46-4.30]	-	-	-		✓		-
L19.2	8.052461	18.12658	4.37 [4.24-4.48]	-	-	-		✓		-

Table A1 *continued*

Table A1 *(continued)*

Arc ID[a]	R.A. [deg]	Decl [deg]	z_{phot} [z_{min}-z_{max}][b]	z_{spec}	z^{LTM}_{model}[68% C.I.][c]	$z^{dPIEeNFW}_{model}$[68% C.I.][c]	LTM/ dPIEeNFW[d]	Lenstool[d]	GLAFIC[d]	RMS[e] [']
L19.3	8.028309	18.131135	3.87 [3.06-4.50]	-	-	-		✓		-
L20.1	8.050102	18.123303	2.43 [0.15-2.90]	-	-	-		✓		-
L20.2	8.051282	18.122912	0.08 [0.05-3.08]	-	-	-		✓		-
G21.1	8.048514	18.107541	1.59 [0.45-2.57]	-	-	-			✓	-
G21.2	8.047208	18.107382	1.58 [0.46-2.55]	-	-	-			✓	-
L22.1	8.035258	18.106743	-	-	-	-		✓		-
L22.2	8.033758	18.107896	-	-	-	-		✓		-

[a] Identification of all multiple images uncovered. Those identified with a "c" refer to less reliable therefore candidate identifications that were not included in our SL models. Systems identified with an "L" or "G" refer to those independently identified by the Lenstool and GLAFIC modelling teams, respectively.

[b] Photometric redshift with upper and lower limits, based on the BPZ estimates from the RELICS catalog with the 95% confidence range; a "-" sign indicates an image for which its z_{phot} could not be measured due to light contamination or poor signal-to-noise ratio.

[c] Redshift prediction based on our LTM and analytical dPIEeNFW best-fit models, respectively.

[d] The symbol ✓ indicates whether a multiple image is used in the SL modeling by the LTM/dPIEeNFW, Lenstool and GLAFIC pipelines.

[e] RMS between the observed and model-predicted multiple images from our LTM best-fit model.

[f] Measured by Dessauges-Zavadsky et al. (2017), considered as a fixed redshift in our SL models.

[g] We fix the redshift of system 7 which is a 'dropout' object.